

## PAPER

# Transient photoconductivity and free carrier dynamics in a monolayer WS<sub>2</sub> probed by time resolved Terahertz spectroscopy

To cite this article: Shujuan Xu *et al* 2019 *Nanotechnology* **30** 265706

View the [article online](#) for updates and enhancements.

## You may also like

- [Iron oxide-based nanomaterials for supercapacitors](#)  
Bingyan Xu, Mingbo Zheng, Hao Tang et al.
- [Recent advances in Sb-based III–V nanowires](#)  
Zhaofeng Gao, Jiamin Sun, Mingming Han et al.
- [Understanding semiconductor nanostructures via advanced electron microscopy and spectroscopy](#)  
Reza R Zamani and Jordi Arbiol



**UNITED THROUGH SCIENCE & TECHNOLOGY**

 **The Electrochemical Society**  
Advancing solid state & electrochemical science & technology


**248th  
ECS Meeting**  
Chicago, IL  
October 12-16, 2025  
*Hilton Chicago*

**Science +  
Technology +  
YOU!**

**SUBMIT  
ABSTRACTS by  
March 28, 2025**

**SUBMIT NOW**

# Transient photoconductivity and free carrier dynamics in a monolayer WS<sub>2</sub> probed by time resolved Terahertz spectroscopy

Shujuan Xu<sup>1,2</sup>, Jin Yang<sup>1,2</sup>, Huachao Jiang<sup>1</sup>, Fuhai Su<sup>1,3,4</sup>  and Zhi Zeng<sup>1,3,4</sup>

<sup>1</sup> Key Laboratory of Materials Physics, Institute of Solid State Physics, Chinese Academy of Sciences, Hefei 230031, People's Republic of China

<sup>2</sup> University of Science and Technology of China, Hefei 230026, People's Republic of China

E-mail: [fhsu@issp.ac.cn](mailto:fhsu@issp.ac.cn) and [zzeng@issp.ac.cn](mailto:zzeng@issp.ac.cn)

Received 2 January 2019, revised 5 March 2019

Accepted for publication 12 March 2019

Published 15 April 2019



## Abstract

The frequency and time resolved conductivity in a photoexcited large-area monolayer tungsten disulfide (WS<sub>2</sub>) have been simultaneously determined by using time-resolved terahertz spectroscopy. We use the Drude–Smith model to successfully reproduce the transient photoconductivity spectra, which demonstrate that localized free carriers, not bounded excitons, are responsible for the THz transport. Upon the optical excitation with 400 nm and 530 nm wavelength, the relaxation dynamics of the free carriers include fast and slow decay components with time constants approximately smaller than 1 ps and between 5–7 ps, respectively. The former sub-picosecond decay is attributed to the charge carrier loss induced by the exciton formation, while both the Auger recombination and the surface trapping can contribute to the slow relaxation.

Keywords: WS<sub>2</sub>, Terahertz, carrier dynamics

## 1. Introduction

Two dimensional (2D) transition metal dichalcogenides (TMDs) with atomically thin layers represent unique features such as valley-selective optical coupling [1–4] and a layer dependent bandstructure [5–7], which make TMDs hold great promise in the application of novel optoelectronic devices [8–11]. These 2D TMDs, including MoS<sub>2</sub>, WSe<sub>2</sub>, WS<sub>2</sub>, etc normally have direct gaps in the visible spectrum and an extraordinary large exciton boundary energy, up to a few hundred meV [6, 7]. Upon photoexcitation with photon energies exceeding the band gap, the unbounded charge carriers and bounded neutral excitons are generated within different time stages in nanostructure semiconductors with a large quantum confinement [12, 13]. The interplay of excitons and free electron–hole pairs provides key roles for the photoelectric behavior

of 2D TMDs compounds. For instance, it is desirable to dissociate the excitons into free carriers in order to create an efficient photocurrent for the application of photodetectors and solar devices [13, 14]. However, it is the excitons rather than the unbound electrons and holes that predominantly determine the photoemission in the 2D TMDs [5].

Therefore, understanding the relaxation dynamics of photoexcited excitons and electron–hole plasma is essential for developing 2D TMD-based photonics and photoelectric devices. A number of pioneering works have been devoted to exploring the ultrafast carrier dynamics such as the transition from hot electron–hole pairs to excitons [15–17], exciton dissociations and annihilations [14, 17–19], exciton diffusion [20], charge carrier transfers [21–23], carrier cooling [24], and excitonic structure renormalization [25, 26] by means of time resolved optical spectroscopy from the visible to mid-infrared spectrum range. In recent years, time resolved terahertz spectroscopy (TRTS) has emerged as an ideal non-contact probe method for carrier dynamics with subpicosecond resolution, benefiting from simultaneous access to the frequency and time resolved

<sup>3</sup> Present address: Key Laboratory of Materials Physics, Institute of Solid State Physics, Chinese Academy of Sciences, Hefei 230031, People's Republic of China.

<sup>4</sup> Authors to whom any correspondence should be addressed.

photoconductivities. Since the THz response is sensitive to the carrier movement and excitonic polarization, TRTS methods have been successfully used to identify the dynamics of free electron–hole pairs and excitons [12, 13, 27–29]. Some TRTS studies on the transient photoconductivity of monolayer and multilayer TMDs have been described [30–36]. C H Lui *et al* observed a transient photoconductivity decrease that originated from the charged trions, i.e. the bound states of two electrons and one hole [30], in a doped monolayer MoS<sub>2</sub>. Most researches on 2D TMDs present the THz photoconductivity increases as having subsequent decays on the timescale from a sub-picosecond to a few hundred picoseconds. These photoconductivity dynamics were normally assigned to different excitation species and different relaxation pathways, including free-carrier trapping and exciton evolutions [31–36]. As far as a monolayer WS<sub>2</sub> is concerned, exciton dynamics such as exciton formation and recombination have been deeply investigated by the transient absorption (TA) or time resolved photoluminescence [17–20, 24, 25]. However, the influence of a free carrier on the carrier dynamics, especially in the stage of coexistence of the electron–hole plasma and the excitons, has not been fully explored yet. Although a few works have addressed the free carrier dynamics in few-layer WS<sub>2</sub> laminate [35, 36] with TRTS, such subjects are still in high demand for further investigations, considering that the TMDs monolayer normally shows quite different carrier dynamics scenarios when compared to the corresponding multilayers [31]. In this work, we carry out detailed investigations on the transient THz photoconductivity in a monolayer WS<sub>2</sub> film grown by chemical vapor deposition (CVD) method using TRTS. We find that the photoconductivity is dominated by free electron–hole plasmas, not excitons, by the optical excitation with photon energy exceeding band gap. The relaxation dynamics in the photoconductivity contain fast and slow decay components with sub-picosecond and a few picoseconds time constants, which have close correspondences to the exciton formation, the surface trapping, and the Auger recombination (AR). Our work provides the insight to the ultrafast dynamics of THz photoconductivity in monolayer WS<sub>2</sub> and it would be valuable for the photoelectric applications of monolayer WS<sub>2</sub>.

## 2. Methods

A monolayer WS<sub>2</sub> thin film was fabricated on a sapphire substrate with the CVD method by SixCarbon Technology company [37]. The substrate had a 0.5 mm thickness and a 20 mm × 10 mm size, on which the WS<sub>2</sub> film was deposited over a 10 mm × 10 mm area. The rest area without a sample was taken as the reference in the measurement. The TRTS setup was similar to references [38–40]. Femtosecond pulses with 45 fs durations, 800 nm wavelengths were delivered from an amplified Ti:sapphire laser system (Coherent Legend) with a repetition rate of 1 kHz. The laser beam was divided into three portions for the generation of THz transients and sampling, as well as for the optical excitation of the sample. The THz pulse was generated via optical rectification in a [110] ZnTe crystal. The sample was placed at the focus of the

THz probe beam and it was photoexcited with a collinear optical pump beam. The pump pulses with wavelengths of 400 and 530 nm were produced with double frequency from a Beta-Barium Borate crystal and parameter conversion from an optical parameter amplifier (TOPAS). The pulse duration was shorter than 100 fs. The spot diameters on the samples for the THz probe beam and the pump beam were about 1.6 mm and 4.2 mm, respectively. The pump fluence was varied between 17 and 115  $\mu\text{J cm}^{-2}$  using neutral density filters. Free-space electro-optic sampling in a second [110] ZnTe crystal was used to coherently detect the THz pulse transmitted through the sample. The optical chopper was placed in either the terahertz generation path for the detection of the THz electric field waveform or the optical pump path in order to record the photoinduced transmission change. The sign of the pump-probe signal for the measured monolayer WS<sub>2</sub> was verified by comparison with the measurement of a standard silicon sample, keeping the same parameter settings of the optical chopper and the lock-in amplifier. All the experiments were performed under a dry nitrogen purge at room temperature.

## 3. Results and discussion

The number of layers of the WS<sub>2</sub> film can be determined by Raman spectroscopy, photoluminescence (PL) and atomic force microscopy. As illustrated in figure 1(a), the measured E<sub>2g</sub><sup>1</sup> and A<sub>1g</sub> Raman modes are consistent with the previous observation in monolayer WS<sub>2</sub> [41]. To examine the spatial distribution of layer number, we measured the Raman spectrum at different sample area. The selected location is marked by A, B and C, respectively, as shown in the inset of figure 1(a). It can be seen that the intensity and Raman shifts of E<sub>2g</sub><sup>1</sup> and A<sub>1g</sub> modes have no obvious changes at different position. Further, the optical micrograph of monolayer WS<sub>2</sub> is presented in the inset of figure 1(c), which show the large uniform area of the sample. The scratches were intentionally introduced to show the contrast between WS<sub>2</sub> thin film and the substrate. The obtained Raman spectra at different area and optical micrograph verify that the substrate is fully covered by monolayer WS<sub>2</sub>. The AFM profile in figure 1(b) shows the step height of about 0.7 nm, which further confirms the monolayer feature of the investigated sample. In figure 1(c), a strong single-peak emission around 617 nm can be seen in the PL spectrum with the excitation of 532 nm laser, which emphasizes the direct optical gap in the WS<sub>2</sub> monolayer [42]. The scanning electron microscopy of figure 1(d) shows that the large area monolayer WS<sub>2</sub> covering the sapphire substrate is composed of inhomogeneous polycrystals. Most grain domains distinguished by SEM have the size larger than 1  $\mu\text{m}$ . From the SEM image, the grain boundary density is estimated as about  $8.2 \times 10^7 \text{ cm}^{-2}$ .

TRTS allows us to directly monitor the time evolution of the photoinduced modulation in the THz transmission, i.e.  $\Delta E(t, t_p) = E(t, t_p) - E_0(t)$ , by varying both the THz gating time ( $t$ ) and the optical pump-THz probe delay ( $t_p$ ). Here the symbols  $E(t, t_p)$  and  $E_0(t)$  denote the THz electric-field waveform passing through the photoexcited and unexcited

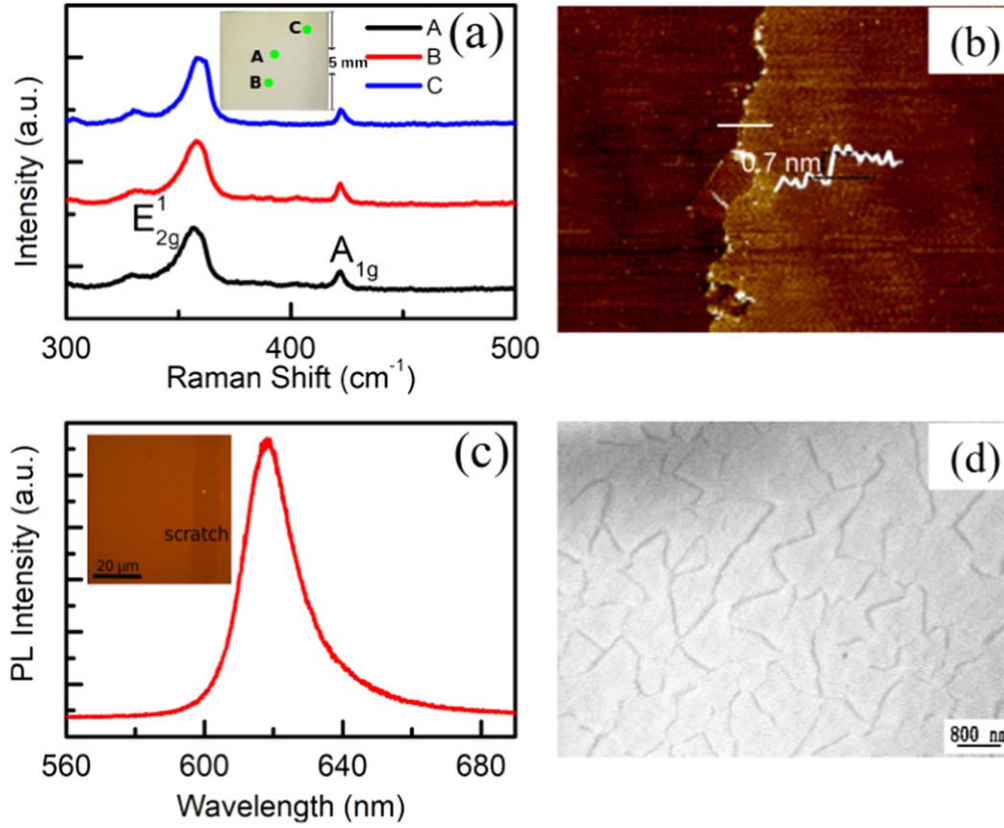


**Figure 1.** Characterization of the monolayer WS<sub>2</sub>. (a) Room-temperature Raman spectra at different position. The inset shows the three different locations on the sample, where the corresponding Raman spectra are taken. (b) AFM image and the corresponding height profile. (c) PL spectra under a 532 nm laser excitation. The inset display optical micrograph of monolayer WS<sub>2</sub>. A purposeful scratch in right side shows the contrast between film and substrate. (d) SEM image of WS<sub>2</sub> samples on the sapphire substrate.

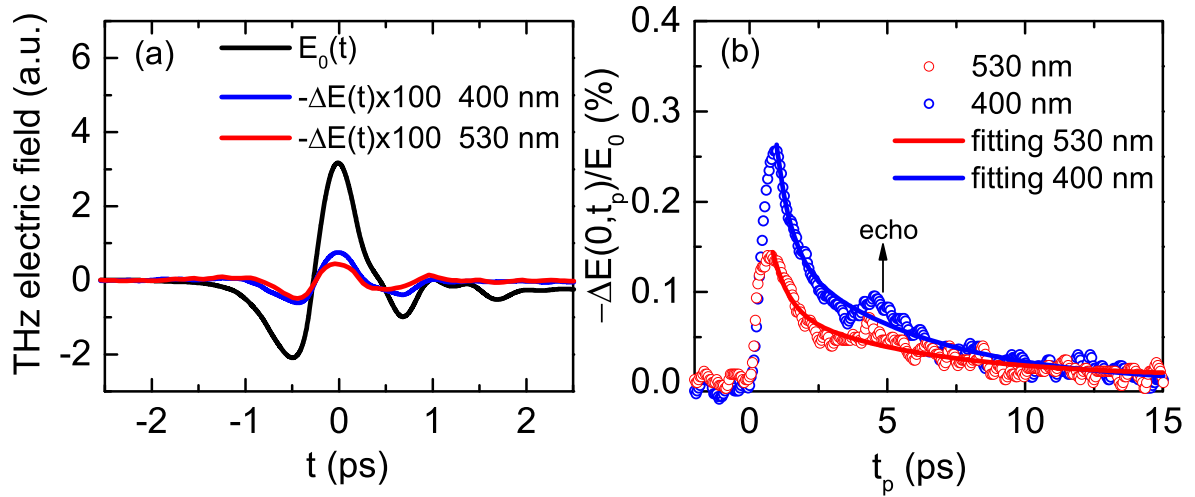


**Figure 2.** (a) Transmitted THz waveform,  $E_0$  without the optical pump and the photoinduced maximum changes,  $-\Delta E(t)$ , at  $t_p = 1$  ps with excitation from wavelengths of 400 and 530 nm. The  $-\Delta E(t)$  waveforms are magnified 100 times for comparison, as denoted by the red and blue lines. (b) The relative change in transmission of the main peak of the THz probe pulse,  $-\Delta E(0, t_p)/E_0$  as a function of the pump-probe time delay,  $t_p$ . The blue open circles and red open circles represent the experimental data from applying the optical pump with wavelengths of 400 and 530 nm. The solid lines are biexponential fits of the data. The 400 and 530 nm laser beam have the same fluence of  $95 \mu\text{J cm}^{-2}$  on the sample.

samples, respectively. In the limit of the small changes in the THz transmission, the transient sheet photoconductivity variety  $\Delta\sigma(t_p)$  can be extracted by measuring the relative

transmission change [43], i.e.

$$\Delta\sigma(t_p) = -\frac{1 + n_s}{Z_0} \frac{\Delta E(t, t_p)}{E_0(t)}, \quad (1)$$



**Table 1.** The determined time constants from the fitting to the carrier dynamics displayed in figure 2(b). The reported time constants in other TMDs are listed for comparison.

Materials	Excitation wavelength (nm)	Fast component (ps)	Slow component (ps)	Very slow component (triexponential fit) (ps)
Mono-WS <sub>2</sub>	400	0.6 ± 0.1	5.4 ± 0.2	—
Mono-WS <sub>2</sub>	530	0.7 ± 0.1	6.0 ± 0.2	—
Few-layer WS <sub>2</sub> [35]	400	~1–2	~22	~107
Mono-MoS <sub>2</sub> [33]	490	0.66 ± 0.15	—	—
Mono-WSe <sub>2</sub> [31]	400	~1	~15	—

where  $n_s$  and  $Z_0$  represent the THz refractive index of the sapphire substrate and the impedance of the free space, respectively. The excitation wavelengths are tuned to 400 and 530 nm, which having photon energies larger than the direct bandgap of monolayer WS<sub>2</sub>. Figure 2(a) presents the  $E_0(t)$  waveform throughout the WS<sub>2</sub> monolayer film on the sapphire substrate, and the corresponding  $-\Delta E(t)$  at  $t_p = 1$  ps after photoexcitation. The transmission changes have been magnified by a factor of 100 for clarification. The incident pump fluences on the sample were set as  $95 \mu\text{J cm}^{-2}$ , which corresponds to the  $1.9 \times 10^{14}$  and  $2.5 \times 10^{14}$  photons  $\text{cm}^{-2}$  for 400 nm and 530 nm wavelength, respectively. By assuming that each absorbed photon injects one pair of electron-hole carriers, we estimate that the optical excitation from 400 nm pump pulse can generate an photoinduced carrier density of about  $2.4 \times 10^{12} \text{ cm}^{-2}$  using an absorption coefficient of  $2.3 \times 10^8 \text{ m}^{-1}$  [42, 44] and considering the pump losses from reflection. The photoexcitation of the sample induced a small decrease in the transmission of the terahertz probe pulse, which indicated that an absence of negative conductivity as observed in the doped monolayer MoS<sub>2</sub> [30]. The 400 nm and 530 nm optical pulses lead to transmission modulations of 0.25% and 0.14%, respectively. It is clear that the 530 nm pump pulse resulted in smaller variety of THz transmission although it had larger incident photon density than 400 nm pump pulse. We measured the temporal evolution of the differential transmission at the main peak of the THz pulse,  $-\Delta E(0, t_p)$ , by fixing the terahertz sampling delay at the maximum of the terahertz field ( $t = 0$  ps) and scanning the pump-probe delay time of  $t_p$ . The normalized transmission change to the maximum value of the THz pulse through the unexcited sample, i.e.  $-\Delta E(0, t_p)/E_0$  is displayed in figure 2(b). The carrier dynamics feature an initial fast rise followed by decay within about 10 picoseconds, which is far shorter than the dynamics observed in few-layer WS<sub>2</sub> laminate using TRTS [35]. An echo signal appears around  $t_p = 4.7$  ps, which is due to the re-photoexcitation of the sample by the multiple reflections of the pump pulse inside the substrate. The carrier relaxation can be reproduced by the biexponential decay function containing fast and slow components. The fitting parameters are put in the table 1. The fast component decays with time constants of  $0.6 \pm 0.1$  ps and  $0.7 \pm 0.1$  ps for the excitation using the 400 nm and 530 nm pulses, respectively. These sub-picosecond fast relaxations are comparable with the observations in other monolayer TMDs such as MoS<sub>2</sub> and WSe<sub>2</sub> in

time constant as shown in table 1. The slow component has lifetimes of  $5.4 \pm 0.2$  ps and  $6.0 \pm 0.2$  ps for the 400 nm and 530 nm excitations, respectively.

Basing on equation (1), the frequency dependent complex photoconductivities at  $t_p = 1$  ps and 3 ps after photoexcitation with a 400 nm optical pulse were obtained using fast Fourier transforms (FFTs). In figure 3, we show typical conductivity spectra under pump fluences of 52, 74, and  $95 \mu\text{J cm}^{-2}$ . The amplitude of the conductivity spectrum is reduced by increasing the pump-probe time delay and decreasing the pump fluence. The positive real conductivities indicate that the free electron-hole plasma dominates the carrier transport in the THz frequency range. Here, we carried out the simulation for the conductivity spectra using the Drude-Smith equation,

$$\sigma_{DS}(\omega) = \frac{ne^2\tau_{DS}}{\mu^*(1 - i\omega\tau_{DS})} \left( 1 + \frac{c_1}{1 - i\omega\tau_{DS}} \right), \quad (2)$$

where  $c_1$  accounts for the extent of carrier localization and backscattering in the thin film,  $n$  is the free carrier density,  $e$  is the electric charge,  $\tau_{DS}$  is the Drude-Smith (DS) scattering time, and  $m^* = 0.16 m_e$  is the effective mass of the carrier [7]. As shown in figure 3, the Drude-Smith model agrees with the experimental results for different time delays and pump fluences. The extracted  $\tau_{DS}$ ,  $c_1$  factor, and  $n$  value from the best fitting under different pump fluence and different pump-probe delays are plotted in figure 4. The  $c_1$  factor does not show obvious fluence dependence and time evolution. The scattering time  $\tau_{DS}$  is reduced lightly with increasing pump fluence, which is likely related to the carrier interaction or heating effect. The saturation of the carrier population can be seen at a high excitation fluence region, as shown in figure 4(a). By applying the pump fluence of  $95 \mu\text{J cm}^{-2}$ , the extracted charge carrier density is around  $2.8 \pm 0.2 \times 10^{11} \text{ cm}^{-2}$  at  $t_p = 1$  ps. Considering the estimated carrier density of  $2.4 \times 10^{12} \text{ cm}^{-2}$  injected by such a pump level, this suggests that only a small fraction of about 12% of the initial excitations leads to the formation of free charges. An amount of excitons are generated, however, they have no contributions to the photoconductivity in our studied frequency region. It is known that both the boundary energy and the intraexcitonic transition of excitons in WS<sub>2</sub> monolayers have energy scales around a few hundred meV [6, 7, 16], which is far larger than our probe frequency range. The excitons behave as a charge neutral insulating gas and they are not able to induce enough polarization changes in the

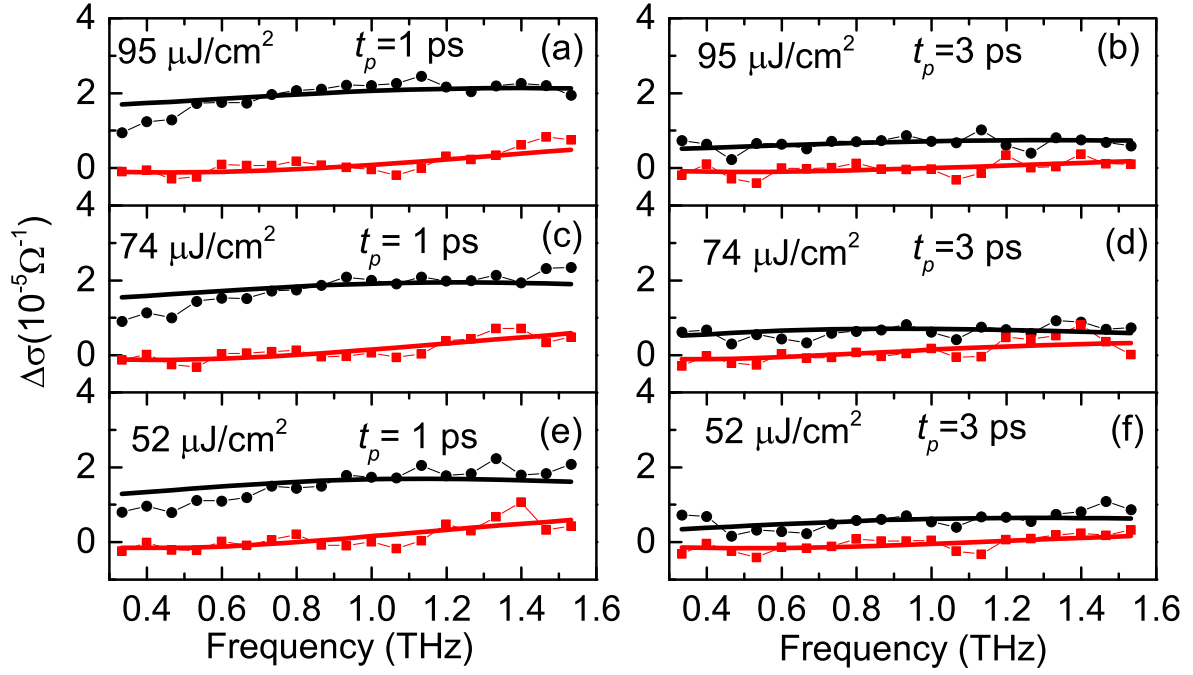


**Figure 3.** Photoinduced changes in the complex conductivity (a) at  $t_p = 1$  ps and (b) at  $t_p = 3$  ps with a pump fluence of  $95 \mu\text{J cm}^{-2}$ , (c) at  $t_p = 1$  ps and (d) at  $t_p = 3$  ps with a pump fluence of  $74 \mu\text{J cm}^{-2}$ , (e) at  $t_p = 1$  ps and (f) at  $t_p = 3$  ps with a pump fluence of  $52 \mu\text{J cm}^{-2}$ . The wavelength of the pump pulse is tuned to 400 nm. The symbols show the experimental real (solid square) and imaginary (solid circle) conductivities, and the solid lines correspond to fittings with the Drude-Smith model.

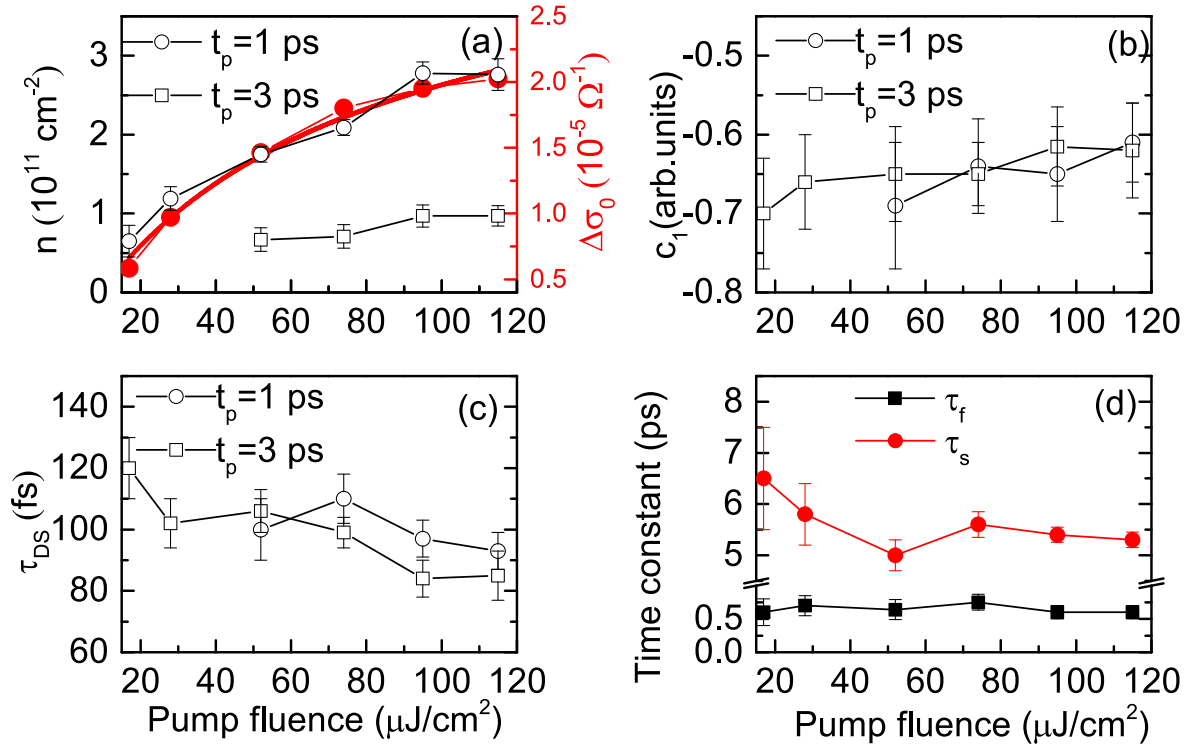


**Figure 4.** (a) The carrier density,  $n$ , (b)  $c_1$  factor and (c) scattering time,  $\tau_{DS}$ , extracted by the Drude-Smith model at  $t_p = 1$  ps (open circle),  $t_p = 3$  ps (open square) after photoexcitation as a function of the pump fluence. The photoinduced maximum real part conductivity change,  $\Delta\sigma_0$ , (solid circle) versus pump fluence is also shown in figure 5(a). The solid lines display the fitting to  $\Delta\sigma_0$  using equation (3). (d) The obtained relaxation time constants as a function of pump fluence, which are obtained by the fittings to the photoconductivity dynamics in figure 5. The solid squares and the solid circles denote the fast and slow decay components, respectively.

measured THz spectrum range. Therefore, it is reasonable to assume that our observed THz transmission change only reflects the carrier transport of the photoinduced electron–hole pairs. In addition, the conductivity spectra dominated by the unbounded carriers do not show pure Drude behavior as seen in monolayer WS<sub>2</sub> flake prepared by mechanical exfoliation [16]. The obtained large  $c_1$  factor ( $c_1 = -0.6$ ) emphasizes the strong carrier backscattering and localized carrier transport in our measured sample. There are different factors, including the carrier backscattering, localized surface plasmon, and excitonic polarization field that can be responsible for the non-Drude conductivity [12, 13, 45, 46]. For instance, it has been found that the excitons contribute to the THz conductivity in the manner of an excitonic polarization field, in which the local restore force is formed and results in the Lorenz resonance of the free carrier in the THz frequency range in few-layer MoS<sub>2</sub> laminate [35]. However, for only the special case of  $c_1 = -1$ , the Drude Smith and Lorenz equations can provide identical conductivity spectra. In our case, the THz conductivity can be well described by the Drude–Smith model with  $c_1$  factor =  $-0.6$ , and it deviates from the Lorenz model. Therefore, it is not clear whether the excitonic polarization field exists in our photoexcited monolayer WS<sub>2</sub>. This feature of partially localization in the THz conductivity can be assigned to the carrier backscattering from the grain boundaries, as shown in the SEM image. The large area monolayer TDMs fabricated by CVD methods has a polycrystalline structure and it is composed of inhomogeneous grains. Therefore, it is reasonable to assume that the conductivity is characterized by a non-Drude shape and localized carrier transport. The weak dependence of the  $c_1$  factor on the pump fluence, as shown in figure 4(b), further excludes the influence of the carrier induced restoring force on the conductivity spectra because both the surface plasma and the excitonic polarization field depend on the carrier density. Because the unbounded carriers dominate the THz conductivity, we can develop an understanding of the dependence of the carrier dynamics on the excitation wavelength, as shown in figure 2. Considering the bandgap of 2.05 eV of WS<sub>2</sub>, the excess kinetic energy of photogenerated carrier is about 1.05 eV and 0.29 eV upon the optical excitation with 400 nm and 530 nm laser pulse, respectively. Therefore, the excitation with a 400 nm photon is able to create nonequilibrium plasma with a higher carrier temperature in comparison to excitation by a 530 nm photon. Such hot carrier tends to prevent the formation of an exciton, and therefore helps to the increase of THz conductivity. As a result, it is reasonable that the photoinduced modulation in the THz transmission is larger for the excitation of a 400 nm photon than for a 530 nm photon.

The real part of photoconductivity obtained from equation (1) as the function of the pump-probe time delays at different pump fluences is plotted in figure 5. The excitation wavelength is 400 nm. It is evident that the THz conductivities show an immediate increase upon photoexcitation and the subsequent decay dynamics of the photoconductivity match biexponential functions for each pump fluence, as shown in figures 5(a)–(f). In figure 4(a), we also present the

maximum value of real part of photoconductivity, i.e.  $\Delta\sigma_0$  as a function of pump fluence. It can be seen that both  $\Delta\sigma_0$  and the carrier density increase nonlinearly with the pump fluence and then arrive at saturation. The pump fluence dependence of  $\Delta\sigma_0$  agrees with the saturable absorber model [19], i.e.

$$\Delta\sigma_0(F) \propto \frac{F}{F + F_s}, \quad (3)$$

where  $F$  is the pump fluence and  $F_s$  is the saturation fluence. The obtained saturation fluence is about  $70 \pm 10 \mu\text{J cm}^{-2}$  from the fitting. It is worth noting that we examined the absorption coefficients by varying the pump fluence. No nonlinear absorption occurred for the sample in the measured pump fluence range. This saturation fluence can inject the total carriers with a density of about  $1.8 \times 10^{12} \text{ cm}^{-2}$ , including both the bound excitons and the free electron–hole pairs. When the photocarrier population approaches the Mott density that corresponds to the intercarrier distance comparable to the excitonic Bohr radius, the Mott transition from the insulating excitonic regime to the electron–hole plasma is expected to occur because of the strong Coulomb screen effect [25, 47]. The Mott density in TDMs has been reported to be higher than  $6 \times 10^{12} \text{ cm}^{-2}$  [25, 47], which is larger than the measured saturation carrier density. In addition, we did not observe any of the remarkable features of the Mott transitions in the conductivity spectra that have been shown in other semiconductors [29]. In contrast to the Mott transition, our observed saturation region likely corresponds to the excitation condition of multi-particle species, e.g. some electron–hole pairs transform into biexcitons [22, 48].

Now we turn to further discussion on the relaxation dynamics of photoconductivity in the THz range. The pump fluence dependent time constants,  $\tau_f$  and  $\tau_s$ , obtained by the biexponential function fittings to the decay curves of the photoconductivities are displayed in figure 4(d). The fast decay component has a subpicosecond time constant that is almost independent of the pump fluence. Paul D. Cunningham *et al* addressed similar photoconductivity dynamics within 600 fs in monolayer MoS<sub>2</sub> using TRTS, in which the fast decay was explained in terms of the charge carrier trapping of the midgap states [33]. In contrast to the single fast decay component in this reference, our observed subpicosecond drop in photoconductivity is followed by a slow component with almost equal amplitude to the fast component. If the fast decay originates from the carrier capture of the trapping states, either all of photoexcited free carriers disappear by rapid trapping in the manner of a single decay component in the low excitation density, or the time constant of the fast decay depends on the pump fluence in the higher excitation density region [15]. Clearly, our observed fast decay has no such hallmarks. Therefore, we can exclude the correspondence between the fast decay and the trapping states. As discussed above, the THz photoconductivity is predominantly contributed by the mobile carriers instead of the bounded excitons. A loss of the free carriers in the population due to the reorganizations into excitons can result in a drop of photoconductivity. It has been well established that the initially excited electron–hole pairs can form into

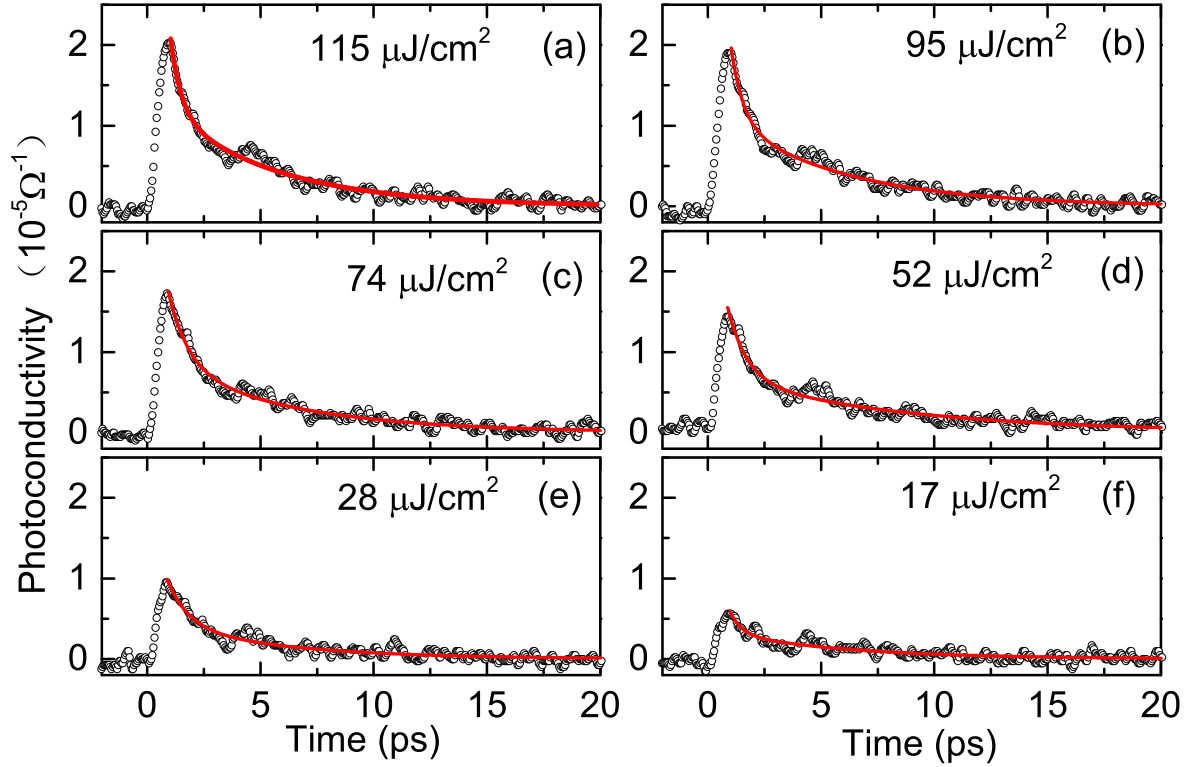


**Figure 5.** The real part of the photoconductivity obtained from equation (1) as a function of pump-probe time delays at different pump fluences. The open circles represent the experimental data. The solid lines show the biexponential fittings for the data. The excitation wavelength is 400 nm.

excitons in the time scale of a subpicosecond in monolayer TDMs such as WS<sub>2</sub>, WSe<sub>2</sub>, using time resolved mid-infrared and TA spectroscopy [15, 16]. In monolayer WSe<sub>2</sub>, P. Steinleitner found that roughly 60% of the injected carriers quickly bound into excitons after 0.4 ps of the above bandgap photoexcitation, and simultaneously the population of the free electron-hole plasma reached a maximum, followed by a subpicosecond drop that originated from the continued transform of the free charge carriers into excitons [16]. We propose that similar carrier evolution dynamics take place in monolayer WS<sub>2</sub> and that the fast decay component arose from the exciton formations.

For slow decay with a time constant around a few picoseconds, the non-radiative recombination pathways such as the AR and the surface trapping should be taken into account. It has been reported that the AR would dominate the exciton dynamics in the 2D WS<sub>2</sub> regardless of the excitation energy for exciton densities greater than  $8.0 \pm 0.6 \times 10^{10} \text{ cm}^{-2}$  and below the Mott density [19]. Our applied pump fluence was able to produce a larger carrier density than this threshold for both the excitons and the free carriers. Therefore, the AR should take a key role for the carrier dynamics. In fact, the time constant of the slow decay component exhibits a slight decrease with increasing pump fluence up to  $52 \mu\text{J cm}^{-2}$ , as shown in figure 5. This pump fluence dependence is in accordance with the behavior of the AR. However, the weak dependence appears when the pump fluence is above  $74 \mu\text{J cm}^{-2}$ . In addition, since the CVD-grown monolayer WS<sub>2</sub> contains nonhomogeneous small

domains and high-density domain boundaries as shown in the SEM, it is expected that surface trapping can contribute to the carrier relaxation. In contrast to the AR, the carrier decay induced by the surface trapping should generally become slower with the increasing pump fluence, due to the filling effects of the available trapping states [15]. We speculate that the surface trapping also contributes to the slow decay in photoconductivity, which competes with the AR process and may counteract the AR induced shortening of the time constant in the high excitation density region.

#### 4. Conclusion

We have carried out detailed investigations of the carrier dynamics of a monolayer WS<sub>2</sub> with sub-picosecond time resolution by employing the TRTS method. Following photoexcitation with 400 or 530 nm optical pulses, the photoconductivity shows fast and slow decay components with time constants of subpicoseconds and 5–7 ps. The fast decay can be explained by the formation of an exciton. However, the slow decay contains both AR and surface trapping dynamics, as supported by the excitation density dependence. The photoconductivity spectra at different time delays after photoexcitation and in the pump fluence range between 17 and  $115 \mu\text{J cm}^{-2}$  have been obtained. We found that the Drude-Smith model could provide decent theory fitting for our experimental results. The calculation emphasizes that a small fraction of photoexcited electron-hole plasma did not



accomplish the formation of excitons within subpicosecond time scale after photoexcitation. These remaining free carriers dominate the THz conductivity even though they are localized by the grain boundary. The pump fluence dependences of the photoconductivity dynamics have been investigated. We found that the initial excited free carrier density and the maximum value of transient photoconductivity show the saturation feature with increasing pump fluence, which may be attributed to the generation of multiple particles. Our work revealed the ultrafast dynamics of free carriers in CVD-grown monolayer WS<sub>2</sub>, and therefore would help the development of ultrafast photoelectric devices based on TMDs materials.

## Acknowledgments

This work was supported by National Natural Science Foundation of China (Grant numbers 11774354, 51727806) and the Chinese Academy of Science (Grant number YZ201524, YZJJ201705).

## ORCID iDs

Fuhai Su  <https://orcid.org/0000-0002-4542-1277>

## References

- [1] Langer F, Schmid C P, Schlauderer S, Gmitra M, Fabian J, Nagler P, Schüller C, Korn T, Hawkins P G and Steiner J T 2018 *Nature* **557** 76–80
- [2] Sie E J 2018 *Science* **355** 1066
- [3] Srivastava A, Sidler M, Allain A V, Lembke D S, Kis A and Imamoglu A 2015 *Nat. Nanotechnol.* **10** 491–6
- [4] Aivazian G, Gong Z, Jones A M, Chu R L, Yan J, Mandrus D G, Zhang C, Cobden D, Yao W and Xu X 2015 *Nat. Phys.* **11** 148–52
- [5] Mak K F, Lee C, Hone J, Shan J and Heinz T F 2010 *Phys. Rev. Lett.* **105** 136805
- [6] Ramasubramaniam A 2012 *Phys. Rev. B* **86** 115409
- [7] Berkelbach T C, Hybertsen M S and Reichman D R 2013 *Phys. Rev. B* **88** 045318
- [8] Yin Z, Li H, Li H, Jiang L, Shi Y, Sun Y, Lu G, Zhang Q, Chen X and Zhang H 2012 *ACS Nano* **6** 74–80
- [9] Lopez-Sanchez O, Lembke D, Kayci M, Radenovic A and Kis A 2013 *Nat. Nanotechnol.* **8** 497
- [10] Baugher B W, Churchill H O, Yang Y and Jarillo-Herrero P 2014 *Nat. Nanotechnol.* **9** 262
- [11] Ross J S et al 2014 *Nat. Nanotechnol.* **9** 268
- [12] Wang F, Shan J, Islam M A, Herman I P, Bonn M and Heinz T F 2006 *Nat. Mater.* **5** 861
- [13] Berggren M R, Palomaki P K, Neale N R, Furtak T E and Beard M C 2016 *ACS Nano* **10** 2316–23
- [14] Steinhoff A, Florian M, Rösner M, Schönhoff G, Wehling T and Jahnke F 2017 *Nat. Commun.* **8** 1166
- [15] Ceballos F, Cui Q, Bellus M Z and Zhao H 2016 *Nanoscale* **8** 11681
- [16] Steinleitner P, Merkl P, Nagler P, Mornhinweg J, Schuller C, Korn T, Chernikov A and Huber R 2017 *Nano Lett.* **17** 1455–60
- [17] Zhao S, He D, He J, Zhang X, Yi L, Wang Y and Zhao H 2018 *Nanoscale* **10** 9538–46
- [18] Yuan L and Huang L 2015 *Nanoscale* **7** 7402–8
- [19] Cunningham P D, McCreary K M and Jonker B T 2016 *J. Phys. Chem. Lett.* **7** 5242–6
- [20] He J, He D, Wang Y, Cui Q, Ceballos F and Zhao H 2015 *Nanoscale* **7** 9526–31
- [21] Hong X, Kim J, Shi S F, Zhang Y, Jin C, Sun Y, Tongay S, Wu J, Zhang Y and Wang F 2014 *Nat. Nanotechnol.* **9** 682
- [22] Chen H et al 2016 *Nat. Commun.* **7** 12512
- [23] Fang Q et al 2018 *J. Phys. Chem. Lett.* **9** 1655–62
- [24] Ruppert C, Chernikov A, Hill H M, Rigosi A F and Heinz T F 2017 *Nano Lett.* **17** 644–51
- [25] Chernikov A, Ruppert C, Hill H M, Rigosi A F and Heinz T F 2015 *Nat. Photon.* **9** 466
- [26] Jiang T, Chen R, Zheng X, Xu Z and Tang Y 2018 *Opt. Express* **26** 859–69
- [27] Hendry E, Schins J M, Candeias L, Siebbeles L and Bonn M 2004 *Phys. Rev. Lett.* **92** 196601
- [28] Suzuki T and Shimano R 2009 *Phys. Rev. Lett.* **103** 057401
- [29] Suzuki T and Shimano R 2012 *Phys. Rev. Lett.* **109** 046402
- [30] Lui C, Frenzel A, Pilon D, Lee Y H, Ling X, Akselrod G, Kong J and Gedik N 2014 *Phys. Rev. Lett.* **113** 166801
- [31] Docherty C J, Parkinson P, Joyce H J, Chiu M H, Chen C H, Lee M Y, Li L J, Herz L M and Johnston M B 2014 *ACS Nano* **8** 11147–53
- [32] Kar S, Su Y, Nair R and Sood A 2015 *ACS Nano* **9** 12004–10
- [33] Cunningham P D, McCreary K M, Hanbicki A T, Currie M, Jonker B T and Hayden L M 2016 *J. Phys. Chem. C* **120** 5819–26
- [34] Liu X, Yu H, Ji Q, Gao Z, Ge S, Qiu J, Liu Z, Zhang Y and Sun D 2016 *2D Mater.* **3** 014001
- [35] Xing X et al 2017 *J. Phys. Chem. C* **121** 20451–7
- [36] Krishna M B M, Madéo J, Urquiza J P, Zhu X, Vinod S, Tiwary C S, Ajayan P M and Dani K M 2018 *Semicond. Sci. Technol.* **33** 084001
- [37] Yan P et al 2017 *Nanoscale* **9** 1871–7
- [38] Cocker T, Titova L, Fourmaux S, Holloway G, Bandulet H C, Brassard D, Kieffer J C, El Khakani M and Hegmann F 2012 *Phys. Rev. B* **85** 155120
- [39] Titova L V, Cocker T L, Cooke D G, Wang X, Meldrum A and Hegmann F A 2011 *Phys. Rev. B* **83** 085403
- [40] Su F et al 2009 *Opt. Express* **17** 9620–9
- [41] Gutiérrez H R, Perea-López N, Elías A L, Berkdemir A, Wang B, Lv R, López-Urías F, Crespi V H, Terrones H and Terrones M 2013 *Nano Lett.* **13** 3447–54
- [42] Zhao W, Ghorannevis Z, Chu L, Toh M, Kloc C, Tan P H and Eda G 2013 *Acs Nano* **7** 791–7
- [43] Tielrooij K, Song J, Jensen S A, Centeno A, Pesquera A, Elorza A Z, Bonn M, Levitov L and Koppens F 2013 *Nat. Phys.* **9** 248
- [44] Bernardi M, Palummo M and Grossman J C 2013 *Nano Lett.* **13** 3664–70
- [45] Joyce H J, Docherty C J, Gao Q, Tan H H, Jagadish C, Lloyd-Hughes J, Herz L M and Johnston M B 2013 *Nanotechnology* **24** 214006
- [46] Cocker T L, Baillie D, Buruma M, Titova L V, Sydora R D, Marsiglio F and Hegmann F A 2017 *Phys. Rev. B* **96** 205439
- [47] Gao S, Liang Y, Spataru C D and Yang L 2016 *Nano Lett.* **16** 5568–73
- [48] You Y, Zhang X X, Berkelbach T C, Hybertsen M S, Reichman D R and Heinz T F 2015 *Nat. Phys.* **11** 477